Nanoscale

PAPER

View Article Online
View Journal | View Issue

Cite this: *Nanoscale*, 2026, **18**, 2751

Visible light photocatalytic ammonia production on single Cu entities attached to nitrogen-deficient functionalized BN sheets

Gulnaz Perveen,[a] Anshu Shrivastava,[a] Uttam Kumar,[a] Nivedita Singh,[a] Harshini V. Annadata,[b] Biplab Ghosh,[b] Mukul Gupta [c] and Indrajit Sinha *[a]

Received 2nd October 2025,
Accepted 9th December 2025

DOI: 10.1039/d5nr04179a

rsc.li/nanoscale

The present research involves the fabrication of a nitrogen-deficient functionalized BN material with isolated Cu–OH groups tethered to it. This material exhibits a visible range indirect band gap (1.52 eV) with its conduction band position conducive to 2-electron nitrogen reduction to the N_2H_2 species. Overall, the nitrogen-deficient BN sheet with isolated Cu–OH entities exhibits enhanced visible light nitrogen reduction reaction (NRR) activity compared to many single-atom photocatalysts. Parallel to this, density functional theory (DFT) calculations are conducted to elucidate the enhancement of interaction between nitrogen and the nitrogen-deficient BN sheet due to nitrogen deficiency. Furthermore, it also points to photocatalytic charge transfer to N_2 through the Cu anchored to the nitrogen-deficient BN framework. Overall, this work highlights the potential of nitrogen-deficient BN systems as templates for novel single transition metal atom photocatalysts and their promise for efficient and sustainable ammonia production under ambient conditions.

1. Introduction

Ammonia is a multipurpose and extensively used chemical with numerous applications in various industries to synthesize fertilizers, explosives, rubbers, plastics, and cooling agents.[1] It is also an excellent energy and hydrogen carrier source because of its higher hydrogen content.[2] A high N≡N first-bond breaking energy of 410 kJ mol^{-1} makes the N_2 molecule highly stable and kinetically inert. High ionization energy (15.85 eV) and poor proton affinity (−1.90 eV) further impede N_2 to NH_3 conversion. The Haber–Bosch process is the conventional method for NH_3 production on a large scale. Still, this process involves very high energy consumption (2% of global energy production) and CO_2 emissions (1.2% of global emissions). Moreover, the process is not environmentally friendly at all.[3] Hence, increasing research is being conducted on more cost-effective and ecologically friendly techniques like photocatalysis and electrocatalysis for the nitrogen reduction reaction (NRR) under ambient conditions. Photocatalysis can be an entirely green and economical process. Nevertheless, developing inexpensive and efficient photocatalysts for these processes has been a significant challenge for the NRR.

Various types of photocatalysts have been explored in the literature for the NRR. These include doped photocatalysts, co-catalyst-loaded systems, heterojunctions, and single-atom photocatalysts (SAPs).[4,5] In this regard, layered two-dimensional (2D) nanosheet materials with vacancies, such as oxygen vacancies (OVs), sulfur vacancies (SVs), and nitrogen vacancies (NVs), have played a dramatic role in photocatalysis.[6] The photocatalytic performance of 2D layered materials has also been enhanced by functionalizing them.[7] Another effective method is to incorporate heteroatoms into these 2D nanomaterials.[8,9] Heterostructure or composite formation with a 2D layered entity can also enhance activity if the band gaps of the components are staggered to each other.[10,11] Notably, OV containing metal-doped TiO_2,[12] MoS_2/CdS heterojunctions having SVs,[13] and NV containing g-C_3N_4 [14] photocatalysts have shown significant NRR activities. A vital step in the NRR is nitrogen adsorption. In this regard, anion vacancies in 2D materials can enhance nitrogen adsorption with improved interfacial charge carrier separation and migration. For instance, photocatalysts with nitrogen vacancies are better for facilitating nitrogen atom adsorption.

Given this background, the present research focuses on developing a photocatalyst for the NRR based on nitrogen-deficient and functionalized boron nitride (BN) sheets. Notably, the design and fabrication of visible light 2D BN photocatalysts for the NRR application have not been reported

[a]*Department of Chemistry, Indian Institute of Technology (BHU), Varanasi 221005, India. E-mail: isinha.apc@iitbhu.ac.in*
[b]*Beamline Development and Application Section, Bhabha Atomic Research Center, Mumbai 400085, India*
[c]*UGC-DAE Consortium for Scientific Research, University Campus, Khandwa Road, Indore, 452 001, India*

in the literature to date. Hexagonal BN (h-BN), the most stable among its polymorphs, has a layered graphite-like structure. While graphite is a nonpolar, homonuclear C–C interlayered structure, h-BN has a highly polar B–N bond.[15] Generally, h-BN does not have photocatalytic activity due to its vast band gap energy (5.5 eV). However, its photocatalytic activity, light absorption efficiency, electronic structure, and band gap energy could be modified by creating defects, vacancies, and functionalization with functional groups such as –H, –OH, –COOH, and NH_2.[16] Wang *et al.* reported that the highly exposed (001) planes of h-BN, passivated with the hydroxyl and amino groups, can reduce the band gap substantially.[14] Moreover, Kumar *et al.* have shown that selective transition metal doping of BN sheets could reduce the band gaps to the visible range level.[17]

Recently, 2D layered nanosheet-based SAPs with different defects/vacancies have garnered attention.[18,19] Nanosheets provide enough surface area for the fine dispersion of atoms. Metal atoms attract the N_2 molecules on the photocatalyst's surface, promoting N_2 interaction for adsorption, activation, and boosting the NRR. SAPs exhibit enhanced effects of the metal atom dispersion on the photocatalysis process by altering the electronic structure of photocatalysts and allowing a lower coordination environment.[20–22] A tiny percentage of a metal precursor is required for synthesizing SAPs. Hence, it is cost-effective and reduces precious metal requirements and adverse effects. Nevertheless, only Liang *et al.*[23] have reported the preparation of Cu single-atom porous BN catalysts to reduce *p*-nitrophenol to *p*-aminophenol. Other reports on single-atom BN catalysts are only computational predictions.[24] Considering the above discussion, this work aims to develop a single transition metal atom stabilized on a BN nanosheet for photocatalytic NRR ammonia synthesis.

Cu exists in different oxidation states (Cu^0, Cu^{1+}, and Cu^{2+}), which is very helpful in electron transfer during the NRR.[25–27] Recently, Chen *et al.* reported 2D BN-supported Cu_2O composites for the NRR as photocatalysts under visible light. In this case, the 2D BN part of the composite only acts as a support because of its large bandgap. Hence, the BN part does not contribute to the composite's photocatalytic activity. The enhancement in NRR photocatalytic activity could be due to the enhanced nitrogen adsorption due to the BN part.[28] The BN part of these composites acts only as a support and is not a photo-catalytically active component. Furthermore, these reports are not on SAPs.

Given the foregoing, we designed and developed an SAP with isolated Cu-based entities attached to 2D BN sheets. We introduced hydroxyl and amino functional groups on the 2D BN nanosheets along with N-deficiency and coordinated single Cu atom-based entities to this structure to reduce its bandgap to the visible range.[7] The nitrogen deficiency of the BN sheets facilitates nitrogen adsorption and N–N bond activation. Nitrogen-deficient BN sheets were fabricated using a method reported by Sunny *et al.*[29] The prepared BN nanosheets were subjected to a modified Hummers method to incorporate hydroxyl and amino functional groups. Finally, combining adsorption and precipitation protocols achieved single Cu atom entities anchoring on the functionalized BN sheets. The prepared materials were characterized by powder X-ray diffraction (XRD), transmission electron microscopy (TEM), X-ray photoelectron spectroscopy (XPS), UV diffuse reflectance spectroscopy (UV-DRS), photoluminescence (PL) spectroscopy, Fourier transform infrared (FTIR) spectroscopy, electron paramagnetic resonance (EPR) spectroscopy and extended X-ray absorption fine structure (EXAFS) techniques. We used the abbreviation CuBN for the prepared nitrogen-deficient functionalized Cu-anchored BN sheets. Photocatalytic ammonia production was evaluated on the prepared CuBN 2D photocatalysts under visible light irradiation, and it was quantified by indophenol blue (IB) and ion chromatography (IC) methods.

Parallel to these experimental investigations, density functional theory (DFT) and time-dependent DFT (TD-DFT) calculations were also carried out on the plausible models of functionalized nitrogen-deficient BN (denoted as NDFBN) sheets and isolated Cu–OH groups anchored on the NDFBN (abbreviated as CuNDFBN) sheets. There were two objectives of DFT calculations. One was to obtain the optimized geometries and the electronic structures of the constructed 2D models. The second aim was to understand the mechanism of N_2 interaction with the CuNDFBN model under ground and excited state conditions. The latter is of critical importance because the N_2 molecule should interact effectively with the excited state highest occupied molecular orbital (HOMO) of the photocatalyst.[30] Such interaction activates the N≡N bond and facilitates ammonia formation.

2. Material synthesis

2.1. Synthesis of boron nitride

Nitrogen-deficient hexagonal boron nitride (h-BN) was synthesized using the calcination method given in ref. 29. Typically, 4.075 g of boric acid and 0.92 g of melamine (9 : 1 molar ratio) were mixed finely, dissolved in 70 mL of distilled water (DW), and sonicated for 3 hours. A milky white colloidal sol was obtained and it was dried to complete dehydration at 70 °C. The latter was placed in an alumina boat crucible and kept in a tubular furnace at 400 °C for five hours. In the next step, the temperature was increased to 600 °C and maintained for three hours. In the last cycle, the temperature was increased to 900 °C and was maintained for five more hours. For all steps, the heating rate was 4 °C min^{--1} with varying heating cycles. After this, the furnace was cooled to room temperature, and a solid white (chunk-like) product was obtained. The solid product was dispersed and washed with ethanol several times to remove unreacted precursors and impurities. Finally, a nitrogen-deficient h-BN powder was obtained.

2.2. Functionalization of boron nitride

The nitrogen-deficient h-BN was next treated with a modified Hummers process, wherein 1 g of the prepared h-BN was mixed with 6 g of $KMnO_4$ (mass ratio of 1 : 6) and ground very

fine with a pestle and mortar. The resulting mixture was poured into a precooled (to 10 °C) acid solution of 13.5 mL of H_3PO_4 and 121.5 mL of H_2SO_4. This reaction mixture was kept at 70 °C for 24 hours with constant stirring.[17,31] The reaction was terminated after 24 hours by adding DW and 8 mL of H_2O_2 with continuous stirring for 30 minutes. The resulting suspension was washed sequentially with DW, HCl, and isopropyl alcohol (IPA), and finally with DW until neutral pH was achieved. This step removes the unreacted compounds. The final suspension was dried at 70 °C to powder form. The obtained product was a functionalized BN (hereafter abbreviated as f-BN) sample.

2.3. Synthesis of CuBN catalysts

Cu-anchored single-atom catalysts on f-BN were synthesized by combining adsorption and precipitation methods. The first step involved suspending 100 mg of f-BN into 50 mL of DW and sonicating for half an hour. After that, a specific amount (x weight percentage of f-BN) of $CuCl_2{\cdot}2H_2O$ was added to the f-BN suspension and the mixture was agitated in a thermostatic shaker at 120 rpm for 12 hours for proper adsorption on the f-BN surface. Four different mixtures with x = 0.2, 0.4, 0.8, and 1.6 were prepared in this way. Next, a sufficient volume of 1 M NaOH was added to the sample to achieve pH 10. The mixture was stirred continuously for three more hours and 0.5 mL of 0.2 M ascorbic acid was added. The stirring was continued for another hour. A light grey suspension was obtained. The product was washed with DW several times and dried at 70 °C. The four CuBN samples prepared this way are denoted as 0.2CuBN, 0.4CuBN, 0.8CuBN, and 1.6CuBN (for x = 0.2, 0.4, 0.8, and 1.6, respectively) in the rest of this research communication.

2.3.1. Ammonia production and photocatalytic activity. Typically, 4 mg of each photocatalyst sample was dispersed in 15 mL of DW containing different sacrificial agents using a bath sonicator for 10 minutes. The aqueous suspension (in a 30 mL glass vial) was placed in the photocatalytic chamber and high-purity N_2 gas (99.99%) was bubbled in the dark for 1 hour to attain adsorption–desorption equilibrium. Next, the aqueous suspension was illuminated with cool white LED visible light (intensity: 1430 W m^{-2}) under continuous stirring and N_2 gas purging. After one hour, the aliquots were filtered with a nylon syringe to separate the photocatalyst and determine the ammonia concentration. The ammonia concentration in the supernatant was determined spectrophotometrically using the indophenol blue method[32,33] and validated by ion chromatography. Fig. S1a and S1b show the UV-vis absorption spectra of ammonia obtained using the indophenol blue method and the standard calibration plot obtained using known ammonium ion concentrations. Photocatalytic experiments were carried out in the presence of methanol, ethanol, glycerol, and sacrificial agents.

2.4. Computational details

2.4.1. DFT and TD-DFT calculations. All the calculations were performed using Gaussian 16 software, and structural models were made using GaussView 6.0 software. DFT and TD-DFT calculations were performed by applying the B3LYP functional (Becke-3-parameter-Lee–Yang–Parr) and the 6-311G basis set.[34] The first step was modeling a functionalized BN sheet (denoted as FBN) containing 80 atoms with GaussView 6.0 software. In this sheet, the OH group passivated the terminal B atoms, while the H atoms passivated the terminal N atoms. The modeled FBN sheet was optimized at the level of theory mentioned above (shown in Fig. S2a). Next, a nitrogen vacancy was created in the FBN model, and this structure was optimized at the same level of theory as earlier. The optimized model at this stage of development is abbreviated as NDFBN (shown in Fig. S2b). Then, a Cu-doped BN sheet with a nitrogen vacancy, B–O–B interaction, and a Cu–OH bond was modeled by incorporating a Cu atom in the place of one N atom in the optimized FBN sheet. As mentioned earlier, the optimized geometry of this model is hereafter denoted as the abbreviation Cu-NDFBN. It should be noted that the model includes B–O–B and Cu–OH bonds because the FTIR results (in the forthcoming section 3.1.6) indicate the presence of these functionalities in the experimentally prepared CuBN samples. Fig. 1a and b show the optimized geometries of two CuNDFBN models. Fig. 1a shows the –Cu–OH group attached to a boron atom near the center of the FBN sheet (denoted as c-CuNDFBN), while the model in Fig. 1b is the optimized geometry for the –Cu–OH group attached to a terminal nitrogen (denoted as t-CuNDFBN). In the second stage, the optimized models were subjected to appropriate single-point TD-DFT calculations to simulate their photo-excited states (E.S). Subsequently, another set of DFT calculations was performed to examine N_2 interaction with the ground-state and photo-excited CuNDFBN models. Natural bond orbital (NBO) analysis was also carried out for charge transfer from donor to acceptor orbitals in related models.

2.5. Material characterization

The photocatalyst samples prepared in this study were analyzed using XRD, HRTEM, XPS, FTIR, EPR, UV-DRS, PL, XAS, and IC characterization techniques. The experimental details for these techniques are provided in Section S2 of the SI.

3. Results and discussion

3.1 Characterization

3.1.1 XRD. XRD data analysis revealed the synthesized photocatalyst's crystalline structure and phase information. Fig. 2a displays the XRD patterns of f-BN and other BN samples with different amounts of the Cu precursor (or CuBN samples). The XRD patterns of all samples have peaks at 26.7°, 41.5°, 43.8°, and 55.16°. This set of peaks corresponds to the (002), (100), (101), (102), (004), and (103) planes, respectively, of h-BN (JCPDS card number 34-0421).[35] The prominent peak at 26.7° represents the formation of graphite-like layered h-BN. Fig. 2b shows that the peak at 26.7° shifts towards the higher 2θ-value for the CuBN samples, indicating that the larger Cu-atom increases the defects in the BN layered structure and decreases the d-spacing of (002) planes.[32,36] No additional

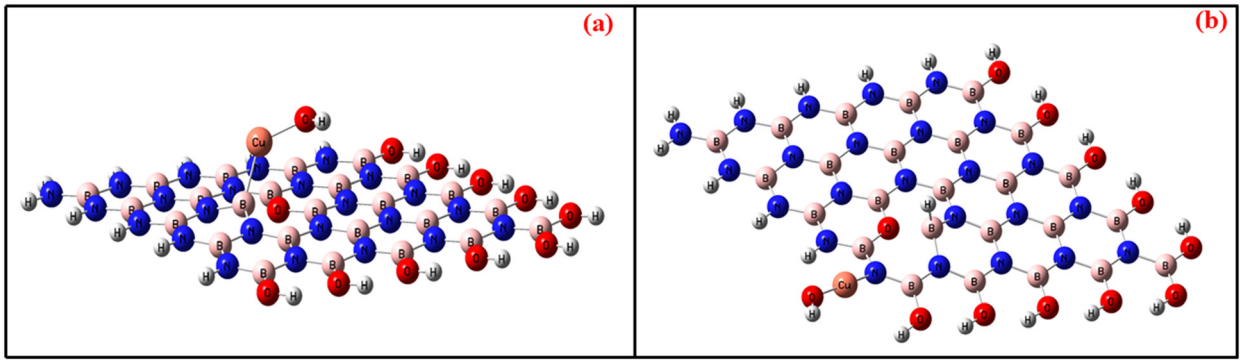

Fig. 1 Optimized structures of (a) c-CuNDFBN and (b) t-CuNDFBN models.

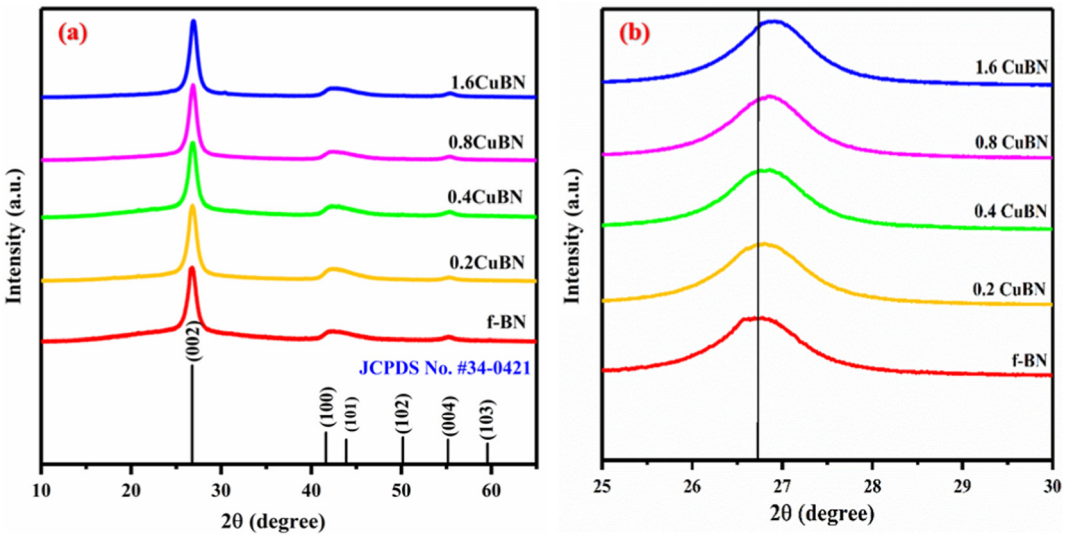

Fig. 2 (a) XRD patterns of f-BN and other CuBN samples and (b) a magnified image showing the shifting of the (002) plane of CuBN samples.

peaks of any other Cu-based phases could be ascertained, indicating that the Cu dopant does not agglomerate or form a separate phase. Hence, one can conclude that Cu is homogeneously distributed in the BN framework.

3.1.2 HR-TEM. Fig. 3a–d show the TEM and HR-TEM images of the h-BN and 0.8CuBN photocatalysts. Fig. 3a and b display the morphologies of the f-BN and 0.8CuBN particles. The f-BN sample has particles in the 8–10 nm size range, while particles in the 0.8CuBN sample also lie in the same range. The histogram plots of the f-BN and 0.8CuBN samples are given in Fig. S3. The HR-TEM images of both f-BN and 0.8CuBN show lattice fringes of ~0.30 nm spacing (Fig. 3c and d), corresponding to the (002) lattice plane. Nanoparticles of both samples have similar shapes and sizes.

3.1.3 XPS. The XPS technique was used to analyze the surface composition and the oxidation states of elements in the prepared photocatalyst. The relative concentration of nitrogen vacancies was determined by the XPS atomic ratio of the B 1s and N 1s elements. The calculated N/B ratio for the f-BN and 0.8CuBN samples was 81.7% and 75.1%, respectively, indicating a significant increase in surface nitrogen vacancies of the 0.8CuBN sample. The XPS atomic percentage values are given in Table S1 in the SI.

Fig. S4(a and b) show the valence band (VB) spectra of the f-BN and 0.8CuBN samples and the effect of Cu-anchoring on the valence edge of the prepared photocatalyst. The VB positions of f-BN and 0.8CuBN are at 2.4 and 0.14 eV, respectively. Fig. S4(c) shows the survey spectra of the f-BN and 0.8CuBN samples, indicating that B, O, N, and Cu elements constitute these samples. A comparison of the high-resolution spectra of the B 1s regions of the f-BN and 0.8CuBN samples is shown in Fig. 4a. The B 1s spectra of the f-BN samples could be curve-fitted to the peak at 190.48 eV (due to the B–N bond) and another lower intensity peak at 191.34 eV for the B–O bond. In the case of the 0.8CuBN sample, the first intense peak remains almost at the same binding energy (BE) at 190.47 eV, whereas the second peak (attributed to the B–O bond) shifted to a slightly higher 191.42 eV BE value. The latter indicates the presence of both B–O–B and B–OH entities in the f-BN and 0.8CuBN samples.[7]

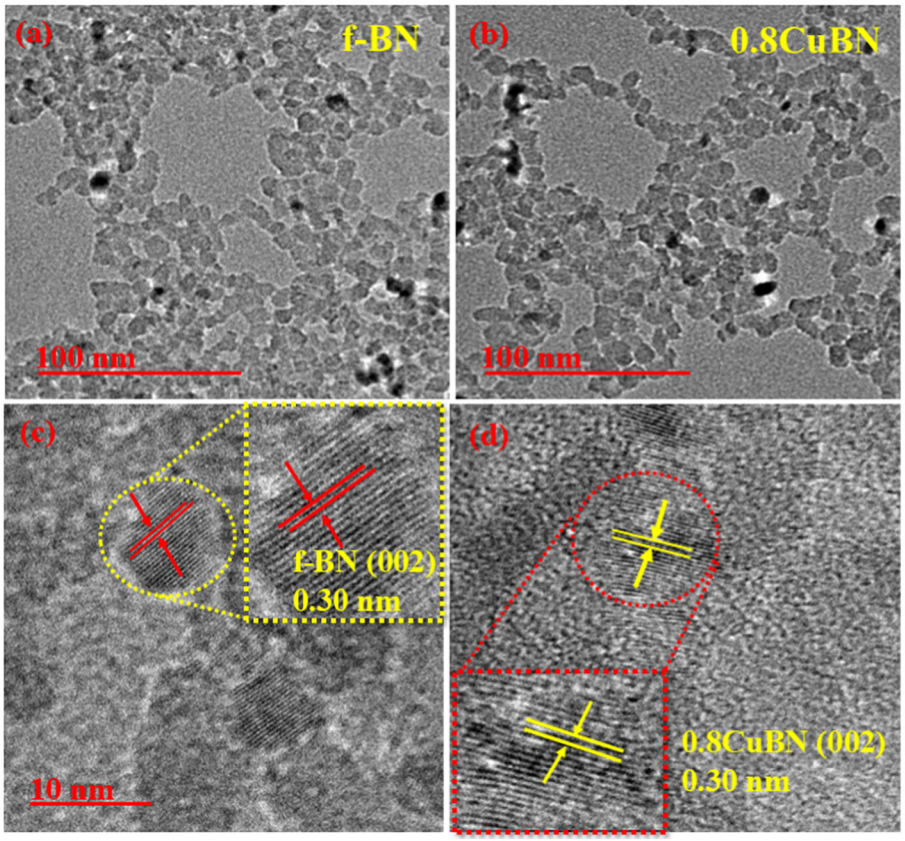

Fig. 3 TEM images of (a) f-BN and (b) 0.8CuBN samples. HR-TEM images of (c) f-BN and (d) 0.8CuBN samples showing typical lattice spacing fringes.

Two peaks were observed at 398.26 and 398.99 eV in the N 1s core spectra of the f-BN sample. These peaks are assigned to the N–B and N–H bonds, respectively. In the 0.8CuBN samples, these peaks appear at 398.11 and 398.97 eV BE, respectively. Both peaks are shifted toward lower BE by 0.2 eV in the 0.8CuBN samples. An overall comparison of the N 1s and O 1s regions of the f-BN and 0.8CuBN samples in the high-resolution spectra shows that CuBN makes the (0.8CuBN) sample electron rich.

The above B 1s and N 1s spectral observations match the FTIR analysis of the f-BN and 0.8CuBN samples.[37] Fig. 4d presents the Cu spectrum of the 0.8CuBN photocatalyst. The two peaks at 933 and 952.8 eV for Cu $2p_{3/2}$ and Cu $2p_{1/2}$ indicate that Cu could be in the +2 oxidation state.[38] The O 1s spectra (Fig. 4c) of f-BN could be deconvoluted into a peak at 532.5 eV and another peak at 533.2 eV. The former indicates the presence of the –OH functional group and the latter points to an O–B bond entity conforming to the B 1s spectral observations.

3.1.4 UV-vis diffuse reflectance spectroscopy. The Kubelka–Munk relation was used to obtain the absorbance plot from the initial solid-state reflectance data of the synthesized materials. Fig. S5a shows the absorbance plots of f-BN and different CuBN photocatalysts and Fig. S5b shows the indirect band gap of all CuBN samples. The band gap decreased with increasing amounts of Cu precursor and exhibited indirect gap values in the range of 1.49–1.55 eV. The band gap energies of these materials were calculated from the Tauc plot (using eqn (1)).[39]

$$(\alpha h\nu)^{1/n} = A(h\nu - E_g) \quad (1)$$

where α and $h\nu$ denote the absorption coefficient and photoelectron energy in the Tauc equation. The value of n is 2 for the indirect transition and $\frac{1}{2}$ for the direct transition. A is a constant and E_g is the band gap of the photocatalyst. Fig. 5a shows that the direct band gap of pristine f-BN is 4.25 eV. The Tauc plot of the 0.8CuBN sample (Fig. 5b) shows a substantially reduced indirect band gap of ~1.52 eV. Using the value of the VB position of the 0.8CuBN photocatalyst (0.14 eV) and the indirect bandgap, we calculated its conduction band (CB) position at −1.38 eV.

3.1.5 Photoluminescence (PL). The photoluminescence (PL) emission spectrum provides insight into the relative charge recombination kinetics of photo-excited photocatalysts. The lower intensity of a PL emission spectrum points to a lower charge recombination rate and, consequently, higher interfacial charge separation. The latter is a prerequisite for improving the photocatalytic activity of the investigated material. Fig. 6 shows the PL emission spectrum recorded at 340 nm emission wavelength. The recorded PL spectrum shows that 0.8CuBN has a lower intensity than an f-BN

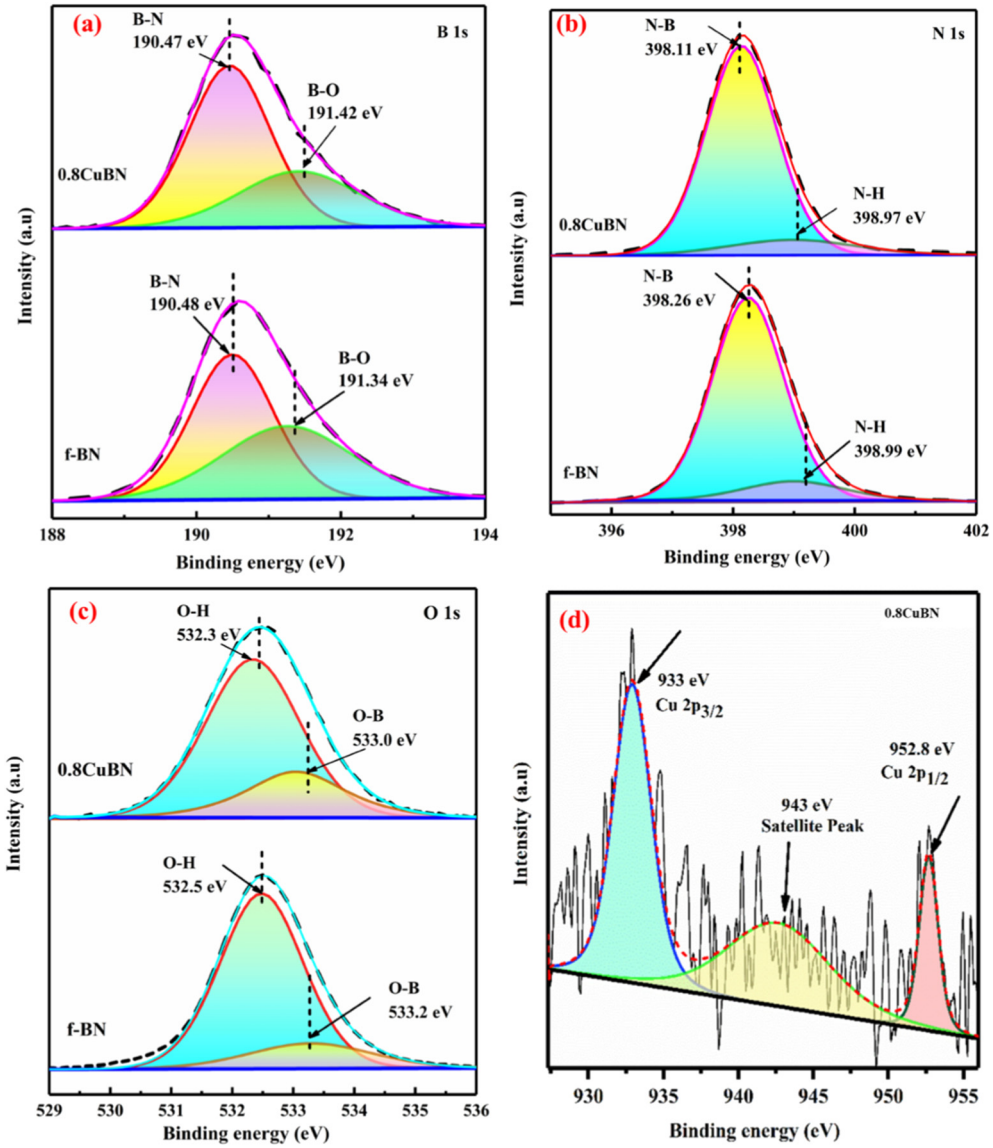

Fig. 4 (a–c) Comparison of the high-resolution B 1s, N 1s, and O 1s spectral regions of f-BN and 0.8CuBN samples. (d) High-resolution Cu 2p spectrum of the 0.8CuBN sample.

sample. Thus, the recombination kinetics of 0.8CuBN is slower than f-BN, indicating its potential for higher photocatalytic activity.

3.1.6 FTIR. Fig. 7 displays the FTIR spectra of the BN-based materials prepared in this research. The transmittance plot (the black curve) due to f-BN exhibits IR bands at ~769, 1380, and 3420 cm^{-1}. The first band (~769 cm^{-1}) is attributed to the out-of-plane B–N–B bending, while the band at 1380 cm^{-1} could be ascribed to either B–N or B–O stretching vibrations.[37,40] Similarly, the peak at 3420 cm^{-1} could be ascribed either to –NH or –OH functional groups. Hence, this analysis points to the presence of B–N–B, B–N, B–O, –NH, and –OH entities in the prepared f-BN sample.

The peak areas of the –NH and –OH functional groups (3420 cm^{-1}) broaden after Cu anchoring. This could be due to the Cu–OH bond, besides the amino and hydroxyl functional groups already in the f-BN structure. Broadening was also observed for the B–N stretching vibration at around ~1380 cm^{-1}. Thus, the FTIR spectrum of the 0.2CuBN sample showed a stretching IR band in the 1200–1350 cm^{-1} range, corresponding to the Cu–OH stretching frequency.[41] The peak is broadened because it overlaps with the B–O stretching mode from 1200 to 1500 cm^{-1}. The broadening of this peak increases with the increasing weight percentage of Cu or Cu–OH formation. Cu anchoring results in an additional peak at around ~460 cm^{-1}, matching with the IR active mode of $Cu(OH)_2$.[42] Overall, the FTIR spectral analysis indicates the presence of both Cu–OH and $Cu(OH)_2$ groups in the Cu-doped f-BN samples. These groups are, in addition to the B–N–B, B–N, B–O, –NH, and –OH entities, already present in the f-BN sample.

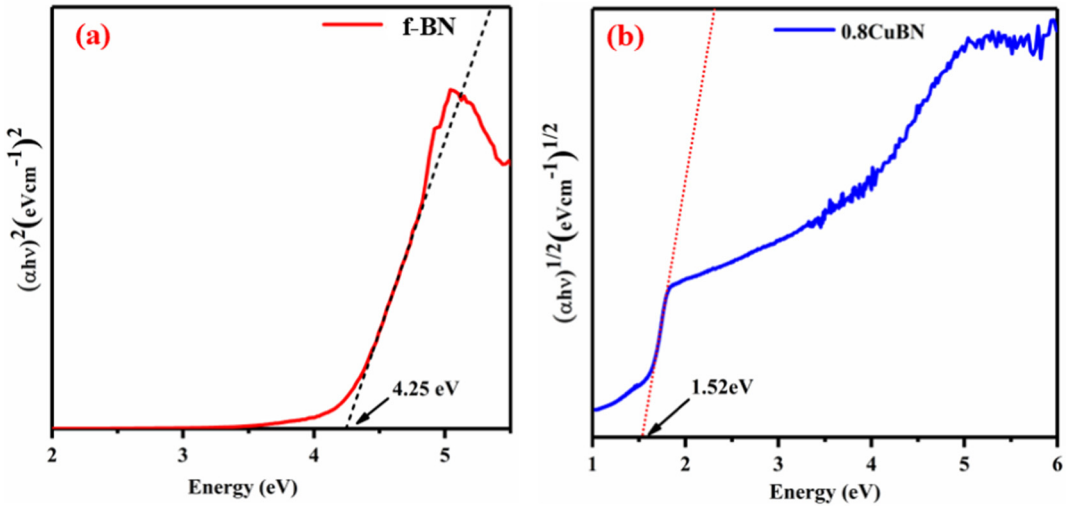

Fig. 5 Tauc plots of (a) f-BN and (b) 0.8CuBN samples.

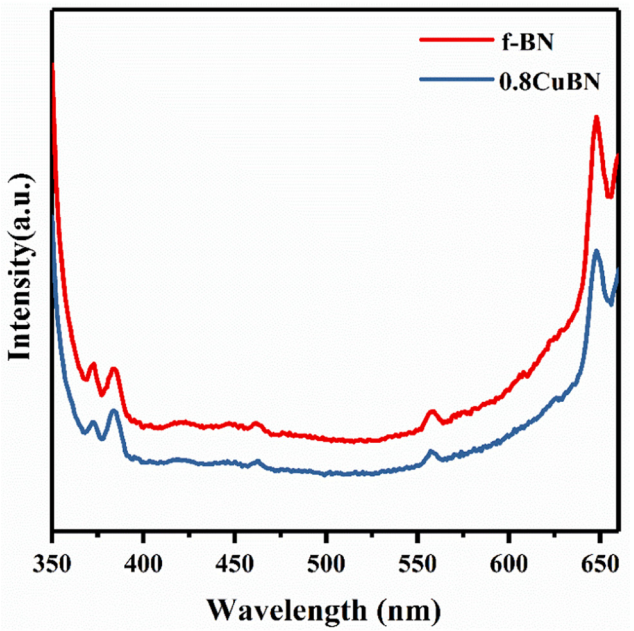

Fig. 6 Photoluminescence (PL) emission spectra of the prepared f-BN and 0.8CuBN samples.

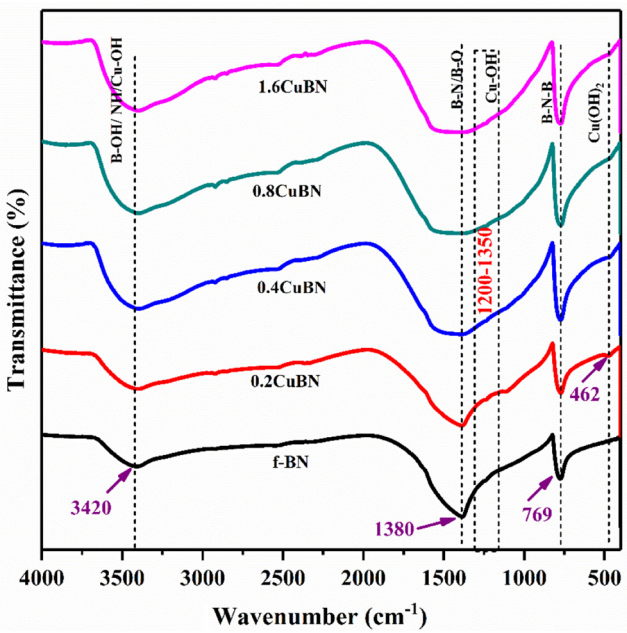

Fig. 7 FTIR spectra of the prepared f-BN and CuBN samples.

3.1.7 Electron paramagnetic resonance (EPR) spectroscopy. Fig. 8 shows the EPR spectra of the solid f-BN and 0.8CuBN samples obtained at ambient temperature. The *g*-value is 1.93 for f-BN and 2.04 for 0.8CuBN in the spectrum. The EPR spectrum of 0.8CuBN is sharper and shifts to a slightly higher *g*-value than that of f-BN. Anchoring of f-BN with the paramagnetic Cu^{2+} species increased the free electron density of the 0.8CuBN samples, resulting in a higher intensity EPR signal and *g*-value than f-BN. Furthermore, Cu incorporation also induced lattice distortion due to the size disparity between Cu^{2+} ions and boron/nitrogen atoms. This, in turn, caused additional nitrogen vacancies (NVs) with free electrons trapped in these vacancies.[43] The negligible EPR signal observed for f-BN and the significantly intensified signal for the 0.8CuBN samples confirm the formation of abundant nitrogen vacancies upon Cu incorporation. Such vacancies induce higher N_2 adsorption activity.

3.1.8 X-ray absorption spectroscopy (XAS) analysis. X-ray absorption spectroscopy was used to investigate the bonding and local structure around an atom in a material. X-ray absorption near edge structure (XANES) analysis was performed for the f-BN sample, while extended X-ray absorption fine structure (EXAFS) analysis was performed for the 0.8CuBN sample. In Fig. 9a and b, the B and N K edge XANES spectra of the

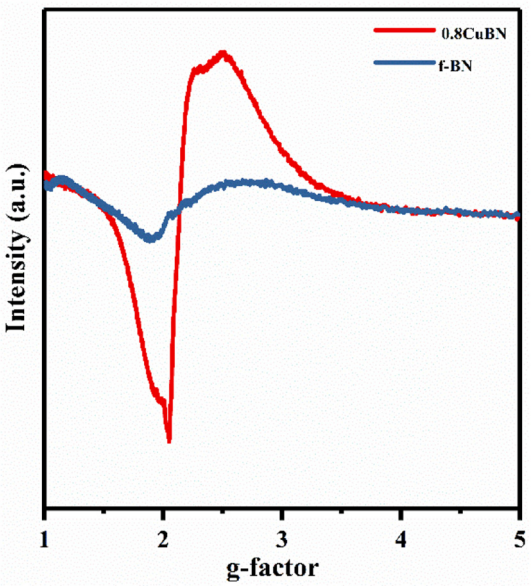

Fig. 8 EPR spectra of f-BN and 0.8CuBN samples.

f-BN sample are shown. It shows a prominent and intense B K edge peak at 192.5 eV due to the B 1s to π* transition. The shoulders in this peak are due to vacancies/defects in the prepared h-BN nanosheets. The higher energy doublet peaks observed at 198 eV and 199 eV are assigned to the B 1s to σ* transition.[44] In Fig. 9b, the main N K edge peak appears at 401.8 eV due to the N 1s to π* transition. This N K edge XANES plot also has a peak at 408.8 eV, ascribed to the N 1s to σ* transition.[45]

3.1.9 Extended X-ray absorption fine structure (EXAFS) analysis. Fig. 10a and b show the EXAFS and the corresponding XANES spectra of the 0.8CuBN (denoted as CuBN in these figures) sample and the Cu foil, CuO (Cu in the +2 oxidation state), Cu_2O (Cu in the +1 oxidation state), and copper phthalocyanine (CuPc) reference samples. The CuPc sample gives the EXAFS reference for the Cu–N bond. A careful examination of Fig. 10b shows that the adsorption edge of CuBN matches best with that of CuO. Moreover, the match of the other reference samples with the absorption edge of CuBN is comparatively poor. It should be noted that XPS analysis also indicated the presence of Cu in the +2 oxidation state.

Fig. 10c displays the Fourier transform spectra of the Cu–K edge EXAFS of four references of Cu foil, CuO, Cu_2O, and CuPc, and the 0.8CuBN sample. The Cu–Cu bond length in the reference Cu foil is greater than 2 Å.[23] No peak matches this in the Fourier transform Cu–K edge plot of 0.8CuBN, demonstrating the absence of Cu–Cu bonding in the prepared sample. A comparison of the 0.8CuBN plot (Fig. 10c) with the remaining shows that the best fit is obtained with the Cu–O plot, indicating that Cu could be in the +2-oxidation state in the sample.

The detailed structural parameters of the 0.8CuBN sample were obtained by fitting the CuBN Fourier transform plot in the R space using Artemis software. It should be noted that the initial fitting parameters were generated (in the Artemis software[46]) by using as input the crystallographic information file (CIF) of the DFT-optimized c-CuNDFBN model structure. Fig. 10d shows the best R-space fit to the 0.8CuBN Fourier transform plot. This fit is obtained using the first coordination shells of Cu–OH (~1.9 Å) and Cu–B (~2.08 Å) bonds, while the second shell is attributed to the Cu–N (~2.91 Å) bond. Table S2 displays the different bond distance values and the corresponding coordination numbers. Since the R space fits the 0.8CuBN Fourier transform plot very well until ~3 Å, we attribute the c-CuNDFBN model structure to the 0.8CuBN sample. Overall, this analysis points to the structure having isolated Cu–OH entities tethered to the NDFBN framework.

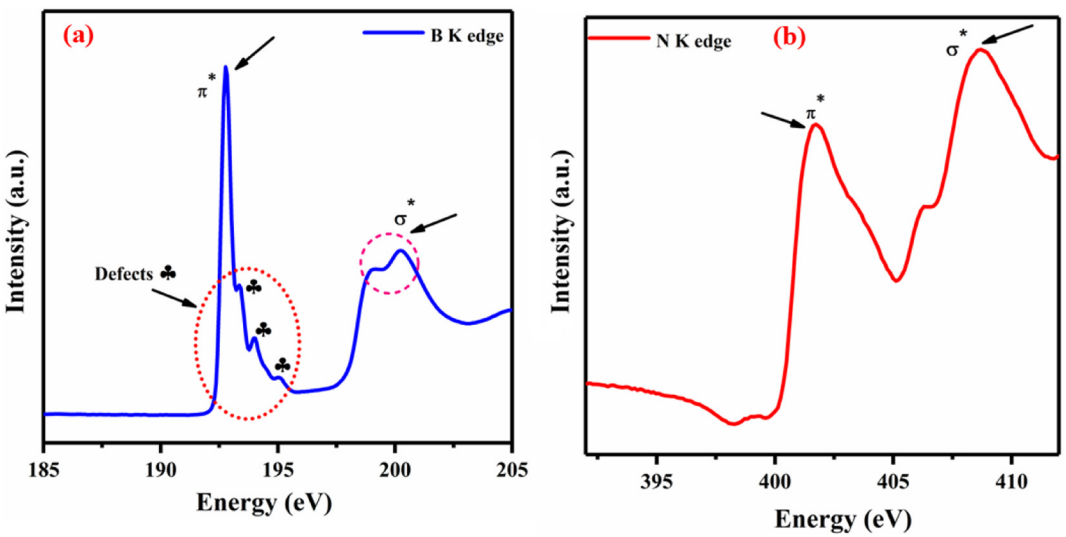

Fig. 9 XANES spectra of (a) the B K edge and (b) N K edge of f-BN.

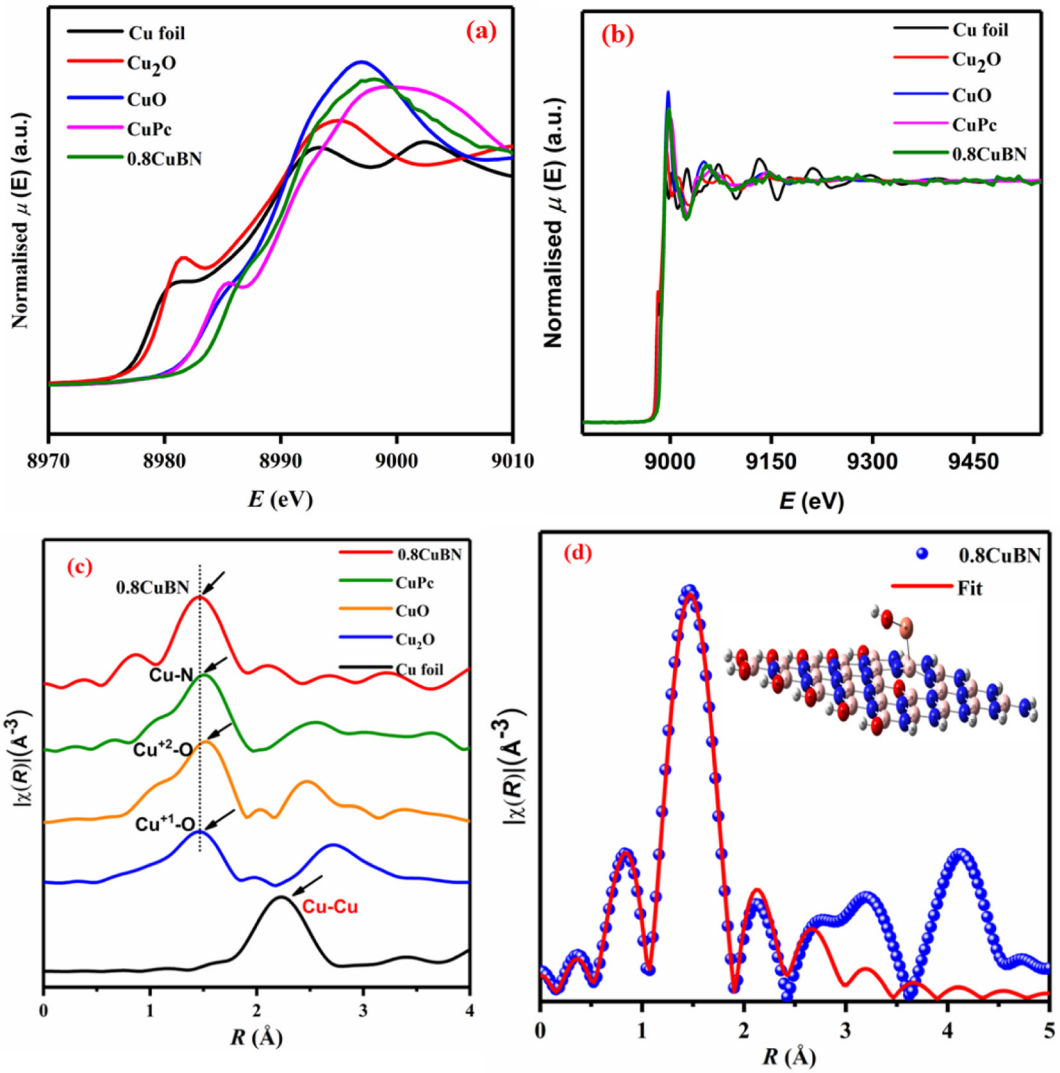

Fig. 10 (a) The normalized Cu K-edge XANES spectra of 0.8CuBN and reference samples, (b) the normalized Cu K-edge EXAFS spectra of 0.8CuBN and reference samples, (c) the Fourier transform spectra of the Cu K-edge EXAFS of 0.8CuBN and reference samples, and (d) the EXAFS fitting curve in the R space.

3.2 The photocatalytic NRR performance of CuBN materials

The photocatalytic NRR was evaluated in an aqueous medium under visible light irradiation with continuous N_2 gas purging on f-BN and all CuBN materials prepared in this study. Two separate techniques, the indophenol blue method and ion chromatography analysis, were used to quantify the concentration of produced ammonium ions. No ammonium ion was detected when a control experiment was performed without a photocatalyst and in the absence of light (under dark conditions). Fig. S6(a) shows the results of photocatalytic control experiments conducted in O_2, Ar, and N_2 environments. The result of the control experiment shows that ammonia production happens only under N_2 purging and no ammonium ions were produced in the O_2 and Ar environments.

Separate photocatalytic experiments were carried out with methanol, ethanol, and glycerol as sacrificial agents. Fig. 11a shows the results of these experiments using 0.8CuBN as the photocatalyst. Ethanol gave the best photocatalytic NRR activity and, therefore, was used as the sacrificial reagent for all other photocatalysis reactions. Fig. 11b exhibits the ammonia production rate on various photocatalysts prepared in this study using ethanol as the sacrificial agent. The f-BN sample exhibited a 30 μmol g^{-1} h^{-1} ammonia production rate. The 0.2CuBN sample exhibited an ammonia production rate of ~65 μmol g^{-1} h^{-1}, while the 0.4CuBN sample showed a considerably higher value of ~130 μmol g^{-1} h^{-1}. The 0.8CuBN sample exhibited the highest ammonia production rate of 159.7 μmol g^{-1} h^{-1}. This photocatalyst gave a five times higher ammonia production rate than pure f-BN. However, the ammonia production activity of the 1.6CuBN sample was only ~81 μmol g^{-1} h^{-1}. Thus, the 0.8CuBN sample exhibited the best ammonia production photocatalytic activity using ethanol as the sacrificial agent. Table S3 shows a com-

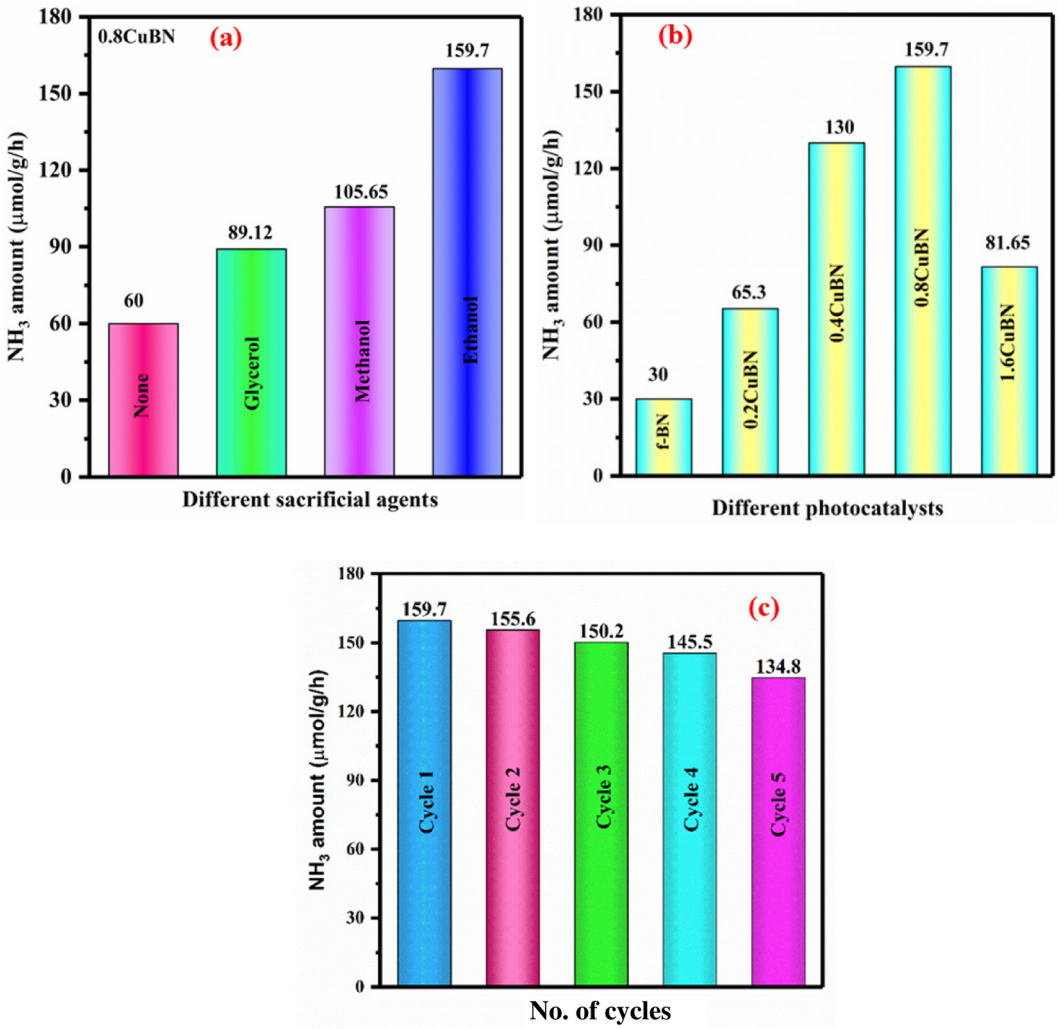

Fig. 11 (a) NRR photocatalytic activity of the 0.8CuBN photocatalyst in the presence of different sacrificial agents, (b) NRR photocatalytic activity of f-BN and different CuBN photocatalysts using ethanol as the sacrificial agent, and (c) a graph showing the recyclability of the 0.8CuBN photocatalyst for NRR activity.

parison of the ammonia production rates of the 0.8CuBN sample with those of samples in the previously published literature. The comparison includes SAPs, metal-doped 2D photocatalysts, layered double hydroxide (LDH), and heterostructure photocatalysts. Among these, the 0.8CuBN sample exhibited a higher yield.

We also conducted N_2 reduction experiments using different photocatalyst loadings (2 mg, 4 mg, and 8 mg) to investigate the effect of catalyst mass on photocatalytic performance. The mass-normalized ammonia production rate (~160 μmol g^{-1} h^{-1}) remained nearly constant across these samples, indicating that the photocatalytic activity is intrinsic to the catalyst and not significantly influenced by the catalyst mass within this range (see Fig. S6c).

The recyclability of any photocatalyst is a critical factor that determines its future practical applicability. Fig. 11c presents the recyclability of 0.8CuBN for five photocatalytic cycles using ethanol as the sacrificial agent. The ammonia production rate decreased slightly from 159.7 μmol g^{-1} h^{-1} to 134.8 μmol g^{-1} h^{-1} by the fifth cycle. Fig. S6b shows the XRD patterns of the 0.8CuBN photocatalyst before and after five cycles of N_2 photoreduction. All peaks in the XRD pattern of the fresh sample also occur in the XRD pattern of the recycled sample, showing that the structural stability remains the same even after five cycles of reuse. EPR spectroscopy was employed to investigate the involvement of photogenerated holes in the reaction. The measurements were conducted under illumination conditions identical to those used in the photocatalytic NRR process using ethanol as the sacrificial agent. As depicted in Fig. S7, the characteristic TEMPO-h^+ (2,2,6,6-tetramethylpiperidinyl-1-oxyl) signal showed the presence of photogenerated holes (h^+) as active species. Notably, the signal intensity of TEMPO decreases progressively with increasing irradiation time, indicating its oxidation to $TEMPO^+$ on the photogenerated h^+.[47,48] These findings indicate that holes serve as the primary reactive species in this system.

3.3 DFT calculations

The interaction of N_2 molecules with both FBN and NDFBN models was investigated. Fig. S8 (a and b) depict the details of the modelled interactions. The result indicated that N_2 exhibited negligible interaction with the FBN system and tended to move away from the FBN sheet. In contrast, N_2 interacted relatively strongly with a boron atom in the NDFBN system. The N_2 bond length changed from 1.11 to 1.17 Å. The corresponding interaction energies for both systems are presented in Table S5, revealing that NDFBN possesses a more negative interaction energy compared to that with the FBN system. Hence, NVs play a critical role in N_2 adsorption and activation.[49–51]

Fig. 12a displays the HOMO and LUMO locations of the c-CuNDFBN model and the values are given in Table S4. In the ground state (GS), the HOMO is located particularly on the Cu–OH functional group, while the LUMO is distributed around the nitrogen vacancy and the boron bound to the Cu in the distorted FBN sheet. We performed TD-DFT calculations to simulate the photoexcited state of the c-CuNDFBN model (Fig. 12b). In this case, the excited state HOMO is still in the Cu–OH part, whereas the LUMO is distributed around the nitrogen vacancy and the B–Cu bond. Fig. S9(a and b) show the ground and the excited state HOMO and LUMO locations of the t-CuNDFBN model and Fig. S9(c and d) show the initial and final N_2 interactions with the t-CuNDFBN model.

We now present the DFT calculation results of N_2 interaction with the ground state c-CuNDFBN and t-CuNDFBN models. The N_2 molecule was placed adjacent to the ground-state HOMO locations of the c-CuNDFBN and t-CuNDFBN models. Unexpectedly, the DFT optimization calculations of N_2 interaction with the c-CuNDFBN model led to the breaking of the B_{25}–Cu–OH bond and the formation of a B_{24}–OH–Cu entity. Fig. S10 shows this phenomenon. The nitrogen molecule interacts with the Cu of the B_{24}–OH–Cu entity through an end-on configuration and it increases the N_2 bond length to 1.15 Å. It should be noted that this length is slightly less due to the interaction with the NDFBN model. Table S5 lists the interaction ener-

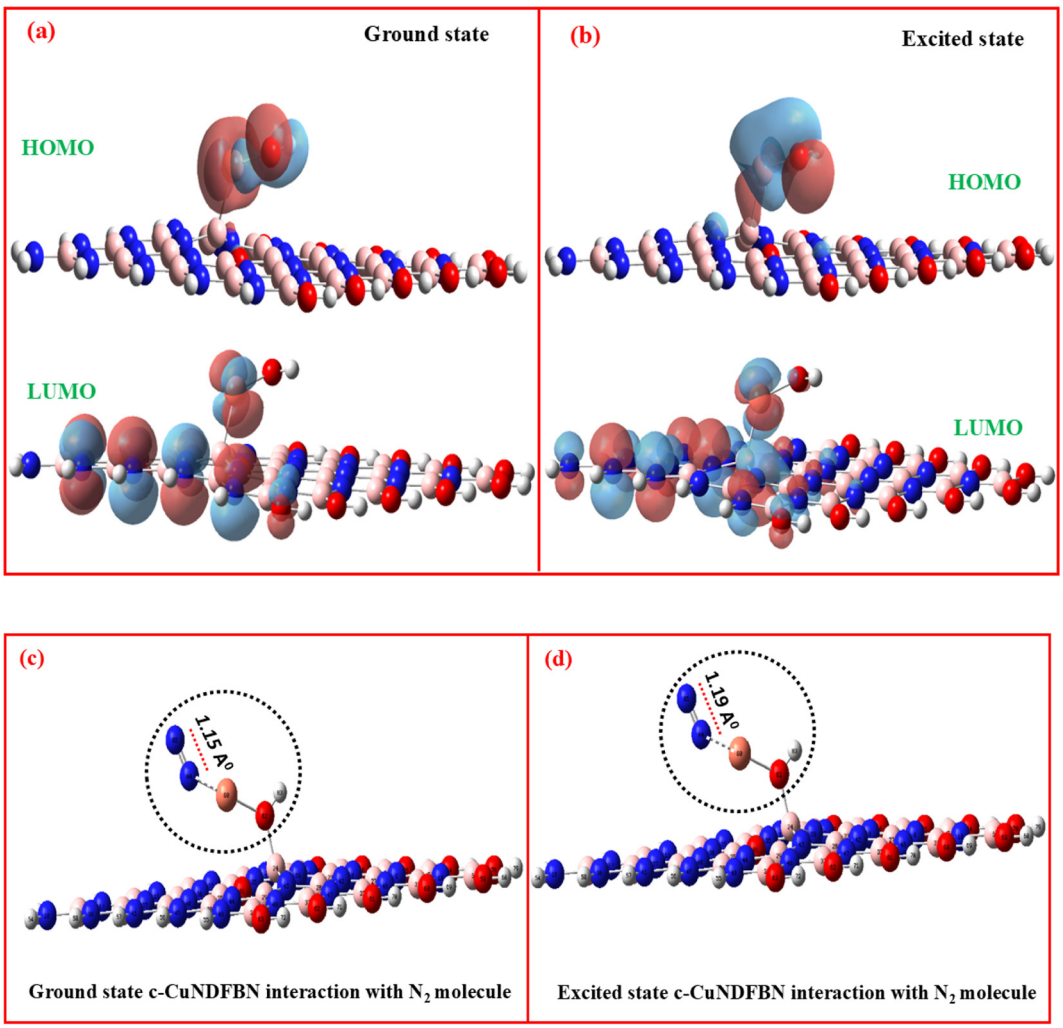

Fig. 12 (a and b) HOMO–LUMO positions of the ground and excited states of c-CuNDFBN and (c and d) N_2 molecule interaction with the ground state and excited states of c-CuNDFBN.

gies of N_2 with the ground states of FBN and NDFBN models. The interaction energy changed from 0.055 to −0.926 eV, showing that the nitrogen deficiency increases the N≡N bond activation significantly. The interaction energy of N_2 with the ground state of the c-CuNDFBN model is more negative (−1.823 eV). Next, we investigated N_2 interaction with the ground state of the t-CuNDFBN model. However, in this case, interaction with N_2 did not cause any change or rearrangement in the structure of the t-CuNDFBN model. The N_2 interaction with the t-CuNDFBN model does elongate the N_2 triple bond to 1.12 Å. Overall, the energy of interaction of N_2 with c-CuNDFBN is more favorable than with the FBN, NDFBN, or t-Cu-NDFBN (Table S5) models.

Given the more favorable interaction of N_2 with c-CuNDFBN, photoexcited state investigations were only carried out on the c-CuNDFBN model. Fig. S11 shows the c-CuNDFBN model's simulated absorption spectrum obtained using TD-DFT calculation. The black vertical lines show the excitation associated with electronic transitions at different wavelengths. The solid blue curve in the same figure represents the experimental solid-state UV-vis spectrum of the 0.8CuBN sample. It should be noted that the calculated UV-vis spectrum of the c-CuNDFBN model does not match perfectly with the experimental solid-state spectrum. This deviation occurs from the inherent limitations of comparing a molecular cluster model with a heterogeneous solid material. In the experimental sample, more than one layer of f-BN sheets is present; as a result, surface defects increase in the experimental samples and electron transfer occurs between adjacent layers. The c-CuNDFBN structure with only one layer is an approximate model of the real CuBN material.

The high intensity absorbance at 748.5 nm in the simulated absorption spectrum is near the absorbance peaks in the experimental UV-vis absorbance curve. Fig. 12b shows the HOMO and LUMO locations of the c-CuNDFBN model corresponding to the 748.5 nm (Fig. S11) photoexcited state. The interaction of N_2 with the excited state of the c-CuNDFBN system results in higher N_2 bond activation and the bond length changes to 1.19 Å (Table S5). This value is close to the HN═NH double bond length (~1.201 Å), suggesting that the NRR photocatalysis system follows the associative mechanism pathway.[6]

3.3.1 Natural bond orbital (NBO) analysis. Natural Bond Orbital (NBO) analysis offers insight into both intramolecular and intermolecular charge transfer mechanisms, providing a detailed understanding of electron density distribution within the system. NBO analysis was also carried out to investigate the N_2 interaction with the ground and excited states of c-CuNDFBN and charge transfer within these entities. The analysis quantifies the charge delocalization relative to the analogous Lewis structure. By applying second-order perturbation theory using the Fock matrix, the second-order delocalization energy $E^{(2)}$ between a donor NBO (i) and an acceptor NBO (j) can be quantified using eqn (2).

$$E^{(2)} = q_i \frac{(F_{i,j})^2}{(\varepsilon_j - \varepsilon_i)} \quad (2)$$

where q_i = donor orbital occupancy, ε_i = energy of acceptor NBO, ε_j = energy of donor NBO and F_i = off-diagonal Fock matrix element. A higher $E^{(2)}$ value signifies a stronger interaction, indicating increased stability of the molecular system due to effective electron transfer between the donor and acceptor orbitals. Table S6 presents the delocalization energy $E^{(2)}$ in kcal mol^{-1} for the c-CuNDFBN system before and after N_2 interaction. Here, LP denotes the 1-center nonbonding lone pair electrons, LP* refers to a 1-center unoccupied (vacant) orbital, BD corresponds to a 2-center bonding (σ) orbital, and BD* denotes a 2-center antibonding σ* orbital.

We begin by discussing the N_2 bond activation resulting from interaction with the ground and excited states of c-CuNDFBN. The ground state c-CuNDFBN shows a charge transfer from the LP (Cu_{80}) to BD* (N_{84}–N_{85}) orbital with $E^{(2)} \sim 2.48$ kcal mol^{-1}. The interaction of N_2 with the c-CuNDFBN ground state also shows an LP(O_{82}) to BD*(Cu_{80}–N_{84}) charge transfer of $E^{(2)} \sim 17.32$ kcal mol^{-1}, along with an LP(N_{85}) to BD*(Cu_{80}–N_{84}) charge transfer of $E^{(2)} \sim 20.67$ kcal mol^{-1}. Overall, there is a charge transfer from the lone pairs of N and O to Cu, which then transfers the charge to the N_2 molecule, resulting in weakening of the N≡N bond to 1.15 Å. In contrast, the excited state of c-CuNDFBN shows an enhanced charge transfer from the LP (Cu_{80}) to BD* (N_{84}–N_{85}) orbital with $E^{(2)} \sim 2.81$ kcal mol^{-1}. The interaction of N_2 with the c-CuNDFBN excited state also shows an LP(O_{82}) to BD*(Cu_{80}–N_{84}) charge transfer of $E^{(2)} \sim 24$ kcal mol^{-1}, along with an LP(N_{85}) to LP*(Cu_{80}) charge transfer of $E^{(2)} \sim 35.18$ kcal mol^{-1}. As can be seen, these charge transfers are larger in magnitude and increase the charge on the Cu, which, in turn, transfers the enhanced charge to the N_2 molecule. As mentioned earlier, this interaction lengthens the N≡N bond length considerably to 1.19 Å.

3.4 N_2 photoreduction mechanism

This section presents a plausible photocatalytic N_2 reduction mechanism based on the experimental and DFT calculation results collated in the preceding sections. The DFT calculations indicate that nitrogen vacancies in the FBN sheets (the NDFBN model) significantly activate the N≡N bond of the nitrogen molecule, increasing it from the normal 1.11 Å to 1.17 Å. Tethering the Cu–OH group to the NDFBN model does not increase N≡N bond activation. Nevertheless, the EPR and XPS results show that Cu incorporation enhances the electron density of the nitrogen-deficient FBN framework. In this context, the DFT calculation results show that N_2 interaction with the photoexcited c-CuNDFBN model activates the N≡N bond more than the NDFBN model and increases it from 1.11 to 1.19 Å. The latter is very close to the HN═NH bond length (1.20 Å).

NBO calculations (section 3.3.1 and the SI) on both the ground and photoexcited states of c-CuNDFBN show charge transfers to the antibonding orbital of Cu–B_{25}, weakening this bond. The charge transfers increase appreciably under photoexcitation. This also increases the electron density of Cu, possibly reducing the latter to a lower oxidation state in the Cu–OH part. The weakening of the Cu–B_{25} bond facilitates Cu interaction with N_2. A strong Cu interaction with N≡N in an end-on fashion ultimately leads to breaking of the Cu–B_{25} bond. At the same time, the oxygen of the Cu–OH part bonds with the adjacent B_{24} site to facilitate charge transfer from the lone

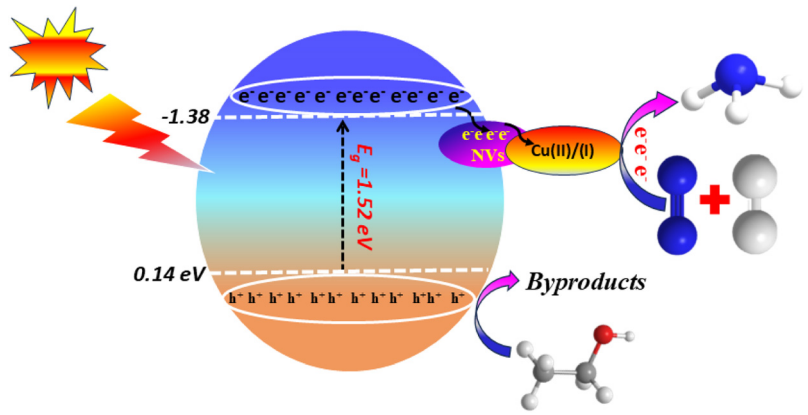

Fig. 13 A schematic of the proposed photocatalytic N_2 reduction mechanism of the CuBN photocatalyst.

pairs of O to Cu, stabilising the B_{24}–OH–Cu rearrangement. Overall, the rearrangement facilitates charge transfer from the lone pairs of O to Cu and subsequently to the N_2 molecule, resulting in weakening of the N≡N bond to a value very close to that of the HN=NH bond length. These results suggest that the dynamic nature of the Cu coordination environment plays a crucial role in enabling efficient electron transfer and intermediate stabilisation during photocatalysis.

We conclude that when the 0.8CuBN photocatalyst is irradiated with visible light from a cool white LED, electrons are photoexcited from its CB system, leaving photogenerated holes in its VB. Moreover, the CB position for the 0.8CuBN photocatalyst is at −1.38 eV, favourable for two-electron N_2 reduction. Likewise, the VB position (~0.14 eV) of the photocatalyst, calculated using its indirect bandgap (1.52 eV), is only suitable for generating hydrogen from an appropriate sacrificial agent, such as ethyl alcohol. As mentioned above, DFT calculations indicate that the –Cu–OH entity rearranges in the presence of N_2 such that the Cu atom interacts strongly with N_2 in an end-on fashion. Parallelly, nitrogen vacancies (NVs) can also capture the photogenerated electrons, suppressing electron–hole recombination (shown in Fig. 13). Due to the comparable size of NVs to that of N_2 molecules, nitrogen is quickly adsorbed onto the NV sites, facilitating its activation.

Based on the CB and VB positions of the 0.8CuBN photocatalyst and the DFT calculation results, we infer a 2-electron nitrogen photoreduction process. Upon accepting two electrons ($2e^-$), N_2 is initially converted into diazine (N_2H_2 in eqn (3)), which subsequently undergoes further reduction by hydrogenation (from the sacrificial agent) to yield ammonia (NH_3) through an alternative associative mechanism pathway.[52]

$$N_2 + 2H^+ + 2e^- \rightarrow N_2H_2, E^0 = -1.10\ \text{V}\ vs.\ \text{NHE} \quad (3)$$

4. Conclusions

Nitrogen-deficient BN sheets decorated with varying Cu contents were prepared and functionalized with hydroxyl and amino functional groups. EXAFS analysis coupled with DFT calculations and characterisation results showed that the isolated Cu–OH entities are bound to the nitrogen-deficient BN framework. Among the prepared BN materials with varying Cu contents, the 0.8CuBN sample exhibited the highest photocatalytic ammonia production activity of 159.7 μmol g^{-1} h^{-1}. Ammonia production was quantified using both ion chromatography and the indophenol blue method. EPR and other techniques showed that the introduction of Cu increased the electron density of the nitrogen-deficient BN sheets.

DFT calculations revealed that nitrogen vacancies in the BN sheets, along with their functionalization, play a crucial role in N_2 adsorption and activation. Moreover, these calculations also indicated that the –Cu–OH group underwent a rearrangement in the presence of N_2. This change led to Cu interacting with N≡N in an end-on configuration. The CB position of 0.8CuBN matches the two-electron photocatalytic N_2 reduction requirement. In addition, the DFT result indicated that the photoexcited charge transfer to N≡N elongates it to almost the N=N bond length. The combination of these inferences led to the conclusion that ammonia formation may occur *via* an associative pathway. Overall, this work highlights the potential of nitrogen-deficient BN systems as templates for novel single-transition-metal-atom photocatalysts and their promise for efficient and sustainable ammonia production under ambient conditions.

Conflicts of interest

There are no conflicts to declare.

Data availability

Data are available upon request from the authors.

Supplementary information (SI) is available. See DOI: https://doi.org/10.1039/d5nr04179a.

Acknowledgements

Gulnaz Perveen gratefully acknowledges the Senior Research Fellowship (SRF) provided by IIT (BHU) for financial support. The authors are also thankful to the Centre for Computational and Information Science CCIS IIT (BHU) for computational facilities. The authors extend their gratitude to CIF, IIT (BHU), for the material characterization facilities. The authors also acknowledge the CRF of the Indian Institute of Technology Delhi (IITD) for providing the EPR facility. The authors acknowledge discussions with Dr Arindam Indra regarding the BN preparation protocols.

References

1 S. Chen, D. Liu and T. Peng, *Sol. RRL*, 2021, **5**, 2000487.
2 Y. Wang, Y. Du, Y. Meng, B. Xie, Z. Ni and S. Xia, *Appl. Surf. Sci.*, 2021, **563**, 150277.
3 Q. Y. Liu, H. D. Wang, R. Tang, Q. Cheng and Y. J. Yuan, *ACS Appl. Nano Mater.*, 2021, **4**, 8674–8679.
4 Q. Han, H. Jiao, L. Xiong and J. Tang, *Mater. Adv.*, 2021, **2**, 564–581.
5 D. L. T. Nguyen, M. A. Tekalgne, T. H. C. Nguyen, M. T. N. Dinh, S. S. Sana, A. N. Grace, M. Shokouhimehr, D. V. N. Vo, C. K. Cheng, C. C. Nguyen, S. Y. Kim and Q. Van Le, *J. Environ. Chem. Eng.*, 2021, **9**, 104997.
6 H. Li, C. Mao, H. Shang, Z. Yang, Z. Ai and L. Zhang, *Nanoscale*, 2018, **10**, 15429–15435.
7 Q. Liu, C. Chen, M. Du, Y. Wu, C. Ren, K. Ding, M. Song and C. Huang, *ACS Appl. Nano Mater.*, 2018, **1**, 4566–4575.
8 J. Zhang, X. Tian, M. Liu, H. Guo, J. Zhou, Q. Fang, Z. Liu, Q. Wu and J. Lou, *J. Am. Chem. Soc.*, 2019, **141**, 19269–19275.
9 H. Wang, J. Wang, R. Zhang, C. Cheng, K. Qiu, Y. Yang, J. Mao, H. Liu, M. Du, C. Dong and X. Du, *ACS Catal.*, 2020, **10**, 4914–4921.
10 T. Saelee, M. Chotsawat, M. Rittiruam, S. Suthirakun, S. Praserthdam, N. Ruankaew, P. Khajondetchairit and A. Junkaew, *Phys. Chem. Chem. Phys.*, 2023, **25**, 5327–5342.
11 S. Wu, Z. Chen, W. Yue, S. Mine, T. Toyao, M. Matsuoka, X. Xi, L. Wang and J. Zhang, *ACS Catal.*, 2021, **11**, 4362–4371.
12 H. Hirakawa, M. Hashimoto, Y. Shiraishi and T. Hirai, *J. Am. Chem. Soc.*, 2017, **139**, 10929–10936.
13 X. Zheng, H. Han, J. Liu, Y. Yang, L. Pan, S. Zhang, S. Meng and S. Chen, *ACS Appl. Energy Mater.*, 2022, **5**, 4475–4485.
14 G. Dong, W. Ho and C. Wang, *J. Mater. Chem. A*, 2015, **3**, 23435–23441.
15 M. S. Meera, S. K. Sasidharan, A. Hossain, J. Kiss, Z. Konya, L. Elias and S. M. A. Shibli, *ACS Appl. Energy Mater.*, 2022, **5**, 3578–3586.
16 J. Ren, L. Stagi and P. Innocenzi, *J. Mater. Sci.*, 2021, **56**, 4053–4079.
17 S. Chahal, T. K. Sahu, S. Kar, S. J. Ray, V. Biju and P. Kumar, *J. Phys. Chem. C*, 2022, **126**, 21084–21093.
18 D. Liu, A. Barbar, T. Najam, M. S. Javed, J. Shen, P. Tsiakaras and X. Cai, *Appl. Catal., B*, 2021, **297**, 120389.
19 L. Zhao, B. Wang and R. Wang, *Adv. Mater. Interfaces*, 2022, **9**, 2200771.
20 T. Hu, G. Jiang, Y. Yan, S. Lan, J. Xie, Q. Zhang and Y. Li, *J. Mater. Sci. Technol.*, 2023, **167**, 248–257.
21 J. Li, P. Liu, Y. Tang, H. Huang, H. Cui, D. Mei and C. Zhong, *ACS Catal.*, 2020, **10**, 2431–2442.
22 S. Liu, Y. Wang, S. Wang, M. You, S. Hong, T. S. Wu, Y. L. Soo, Z. Zhao, G. Jiang, J. Qiu, B. Wang and Z. Sun, *ACS Sustainable Chem. Eng.*, 2019, **7**, 6813–6820.
23 J. Liang, Q. Song, J. Wu, Q. Lei, J. Li, W. Zhang, Z. Huang, T. Kang, H. Xu, P. Wang, X. Zhou, P. K. Wong, H. Li, X. Meng, Z. Jiang and C. S. Lee, *ACS Nano*, 2022, **16**, 4152–4161.
24 Z. Ma, Z. Cui, C. Xiao, W. Dai, Y. Lv, Q. Li and R. Sa, *Nanoscale*, 2020, **12**, 1541–1550.
25 P. Liu, H. Wang, X. Li, M. Rui and H. Zeng, *RSC Adv.*, 2015, **5**, 79738–79745.
26 H. Zhang, Y. Chen, Y. Pan, L. Bao and J. Ge, *J. Colloid Interface Sci.*, 2023, **642**, 470–478.
27 L. Li, C. Hu, L. Zhang, G. Yu, L. Lyu, F. Li and N. Jiang, *J. Mater. Chem. A*, 2019, **7**, 6946–6956.
28 L. Chen, M. Liu, Y. Chen, S. Zhu, C. Sun, X. Tu and H. Zheng, *Catal. Sci. Technol.*, 2023, **13**, 2802–2809.
29 A. Sunny, A. Balapure, R. Ganesan and R. Thamankar, *ACS Omega*, 2022, **7**, 33926–33933.
30 P. V. Nhat, N. V. A. Duy, T. N. Tran, N. T. Si, T. A. Nguyen, N. T. Van, N. Van Nghia, P. Schall, V. A. Dinh and M. T. Dang, *ACS Omega*, 2024, **9**, 20056–20065.
31 W. Gao, Y. Zhao and H. Yin, *RSC Adv.*, 2018, **8**, 5976–5983.
32 Y. Soo, Z. Zhao, G. Jiang, J. Qiu and B. Wang, *ACS Sustainable Chem. Eng.*, 2019, **7**, 6813–6820.
33 T. Hou, Q. Li, Y. Zhang, W. Zhu, K. Yu, S. Wang, Q. Xu, S. Liang and L. Wang, *Appl. Catal., B*, 2020, **273**, 119072.
34 C. Ma, B. Liu and S. Yan, *Mol. Catal.*, 2020, **495**, 111165.
35 A. Sunny, A. Balapure, R. Ganesan and R. Thamankar, *ACS Omega*, 2022, **7**, 33926–33933.
36 W. Lei, D. Portehault, R. Dimova and M. Antonietti, *J. Am. Chem. Soc.*, 2011, **133**, 7121–7127.
37 Y. R. Zhi, B. Yu, A. C. Y. Yuen, J. Liang, L. Q. Wang, W. Yang, H. D. Lu and G. H. Yeoh, *ACS Omega*, 2018, **3**, 14942–14952.
38 Z. Zhang, F. Li, G. Li, R. Li, Y. Wang, Y. Wang, X. Zhang, L. Zhang, F. Li, J. Liu and C. Fan, *J. Solid State Chem.*, 2022, **310**, 123041.
39 B. D. Viezbicke, S. Patel, B. E. Davis and D. P. Birnie, *Phys. Status Solidi B*, 2015, **252**, 1700–1710.
40 S. Li, X. Lu, Y. Lou, K. Liu and B. Zou, *ACS Omega*, 2021, **6**, 27814–27822.
41 R. H. P. Devamani and M. Alagar, *Nano. Biomed. Eng.*, 2013, **5**(3), 116–120.
42 K. Okada, R. Ricco, Y. Tokudome, M. J. Styles, A. J. Hill, M. Takahashi and P. Falcaro, *Adv. Funct. Mater.*, 2014, **24**, 1969–1977.
43 C. Lv, Y. Qian, C. Yan, Y. Ding, Y. Liu, G. Chen and G. Yu, *Angew. Chem.*, 2018, **130**, 10403–10407.

44 N. L. McDougall, J. G. Partridge, R. J. Nicholls, S. P. Russo and D. G. McCulloch, *Phys. Rev. B*, 2017, **96**, 144106.
45 J. Wang, Z. Wang, H. Cho, M. J. Kim, T. K. Sham and X. Sun, *Nanoscale*, 2015, **7**, 1718–1724.
46 B. Ravel and M. Newville, *J. Synchrotron Radiat.*, 2005, **12**, 537–541.
47 W. Chen, J. Huang, Z. C. He, X. Ji, Y. F. Zhang, H. L. Sun, K. Wang and Z. W. Su, *Sep. Purif. Technol.*, 2021, **277**, 119461.
48 P. J. Wright and A. M. English, *J. Am. Chem. Soc.*, 2003, **125**, 8655–8665.
49 Y. Xue, C. Ma, Q. Yang, X. Wang, S. An, X. Zhang and J. Tian, *Chem. Eng. J.*, 2023, **457**, 141146.
50 S. Yu, Z. Mei, L. Wang, Y. Ren, W. Wu, M. Liu, T. Wang and C. Liu, *Nanoscale*, 2025, 11426–11433.
51 D. Zhang, Y. L. Pak, X. Li, S. Lv, M. Xing, Z. Yang, H. Wu, X. Gao, H. Mou and J. Song, *J. Alloys Compd.*, 2024, **972**, 172881.
52 C. J. M. Van Der Ham, M. T. M. Koper and D. G. H. Hetterscheid, *Chem. Soc. Rev.*, 2014, **43**, 5183–5191.